## scientific reports



### **OPEN**

# On the heterogeneous microstructure and strengthening mechanisms in a laser welding AZ80 magnesium alloy

Yu Liu¹, Gaoming Zhu¹,²⊠, Yaqi Wang³, Zhifeng Xin⁴, Ning Hao⁴, Wei Huang⁴, Sangbong Yi⁵, Dietmar Letzig², Ulrich Lienert⁶, Jie Wang¹☒ & Xiaoqin Zeng¹☒

This study investigates the microstructural characteristics and mechanical properties of a laser welded AZ80 magnesium alloy. The welding process led to the formation of coarse-grained fusion zone (FZ), where a secondary phase formed continuous network.  ${\rm Mg_{17}Al_{12}}$  precipitation and coarsening of grain boundaries occurred in the heat affected zone. The welded joint exhibited excellent mechanical properties with a yield strength of 202 MPa and a joint efficiency of 92%. The microstructure analysis via EPMA and EBSD in conjunction with synchrotron X-ray diffraction analysis reveals that precipitates and increased dislocation density in the fusion zone are primary strengthening mechanisms for the laser welded AZ80 Mg alloy.

Keywords Magnesium alloy, Laser welding, Mechanical properties, Synchrotron X-ray diffraction

As an ideal lightweight metal structural material, magnesium (Mg) alloys conform to the concept of modern lightweight, energy saving and emission reduction and have been increasingly evaluated for application in aerospace, transportation, electronic communications, and other industries<sup>1–3</sup>. However, wide usage of Mg alloys in various fields needs the development of processing technologies, and welding is necessary for the manufacturing of wrought Mg alloys parts and the repairing of casting defects<sup>4–6</sup>.

Welding problems, such as joining Mg alloys to themselves and joining Mg to steel or aluminum, have been receiving attention in recent years. Various welding processes, such as tungsten inert gas welding (TIG)<sup>7</sup>, electron beam welding (EBW)<sup>8</sup>, friction stir welding (FSW)<sup>9</sup>, and laser beam welding (LBW)<sup>10</sup>, have been employed for connecting of Mg alloys. Laser welding, in particular, offers advantages over other welding methods, such as high-power density, simple equipment, high welding efficiency, low residual stress in joints, and narrow heat affected zone<sup>11–13</sup>. These advantages position laser welding as a promising technique with broad prospects for joining Mg alloy components.

Mg alloys manufactured by different processes have different weldabilities, and the microstructure and the properties of laser welding also differ. At present, laser welding is mainly applied on wrought Mg alloys, which have demonstrated good laser weldability<sup>14</sup>. Shen et al. <sup>15</sup> investigated the effect of welding speed on the microstructure and mechanical properties of AZ61 Mg alloy using laser welding. It was found that increased welding speed led to the improved strength and elongation of the joint due to the fine  $\alpha$ -Mg equiaxed dendrite crystals and dispersed  $\beta$ -Mg<sub>17</sub>Al<sub>12</sub> particles. In a study of AM80 laser welded joints, Shi et al. <sup>16</sup> achieved excellent joint strength by optimizing the peak power. The tensile strength of the welded joint can reach 142.5 MPa, which is 90% strength of the base material.

The strength of Mg alloy welded joints reported in the literature is generally weaker than that of the base material, which is usually caused by the microstructural differences between the joints and the base material <sup>17–19</sup>. However, insufficient attention was paid to the microstructure of the laser welded joint of Mg alloys (such

<sup>1</sup>National Engineering Research Center of Light Alloy Net Forming & State Key Laboratory of Metal Matrix Composites, Shanghai Jiao Tong University, Shanghai 200240, China. <sup>2</sup>Institute of Material and Process Design, Helmholtz-Zentrum Hereon, 21502 Geesthacht, Germany. <sup>3</sup>Shanghai Key Laboratory of Materials Laser Processing and Modification, School of Materials Science and Engineering, Shanghai Jiao Tong University, Shanghai 200240, China. <sup>4</sup>Consumer & SMB Notebook Development Center, Lenovo (Beijing) Ltd., Beijing 100094, China. <sup>5</sup>School of Materials Science and Engineering, Kumoh National Institute of Technology, Gyeongbuk 39177, South Korea. <sup>6</sup>Deutsches Elektronen-Synchrotron (DESY), 22607 Hamburg, Germany. <sup>™</sup>email: zgm900613@sjtu.edu.cn; gaoming.zhu@hereon.de; wjie\_no1@sjtu.edu.cn; xqzeng@sjtu.edu.cn

as, grain structure, precipitation, and texture). Understanding the microstructure evolution and mechanical behavior of the welding joint is of importance to optimize the welding process. In this study, laser welding was performed on an extruded AZ80 Mg alloy with the objective to correlate the microstructure with the mechanical properties of the laser welded material.

#### Materials and methods Materials preparation

Commercial pure Mg (99.5%), pure Al (99.7%), and pure Zn (99.8%) were used for the melting of Mg-8Al-0.5Zn alloy through semi-continuous casting method. The cast billets with a diameter of 200 mm were homogenized at 350 °C for 24 h and then hot extruded at 380 °C with an extrusion speed of 2 m min<sup>-1</sup> to produce extrusion plate with a dimension of 230 (Width) ×10 (Thickness) mm. The as-extruded alloy was further solid solution treated (T4) at 400 °C for 5 h. Figure S1(a) reveals the microstructure of the as-extruded AZ80 alloy after T4 treatment. The material demonstrates a fully dynamic recrystallized (DRXed) grain structure. No secondary phases were observed from the optical micrograph. Figure S1(b) shows the X-ray diffraction (XRD) result of the AZ80-T4 alloy. Only  $\alpha$ -Mg phase was identified from the diffraction peaks, further confirming the single phase of the investigated alloy.

#### Laser welding process

Rectangular plates with a geometry of  $50 \times 50 \times 2.5$  mm<sup>3</sup> were sectioned by electrical discharge machining (EDM) from bulk extrusion alloy for laser welding. Prior to welding, the surfaces of the plates were properly cleaned by mechanical polishing and acetone cleaning. Figure S1(c) shows the schematic of the laser welding process, with the welding direction aligned along the extrusion direction (ED). The laser power used was 1500 W, the laser inclination was set as 7°, the welding speed was 4.5 mm min<sup>-1</sup>, and the defocus was maintained at zero. Argon was used as protective gas during welding with a flow rate of 25 L min<sup>-1</sup>. Microstructure of the welded joint is shown in Fig. S1(d) that demonstrates good welding quality without obvious porosities and inclusions.

#### Microstructure characterization and mechanical testing

Synchrotron X-ray diffraction experiments were conducted at beamline P21.2 of the PETRA III facility at the Deutsches Elektronen-Synchrotron (DESY) using an energy of 82 keV. The beam size was set to  $150 \times 150 \, \mu \text{m}^2$  to capture information from specific regions of the welded material. The diffraction patterns were analyzed using the open-source software pyFAI (https://github.com/kif/pyFAI).

The microstructure of the welded joints was characterized using optical microscopy (OM, Zeiss), scanning electron microscopy (SEM, Tescan), and electron backscatter diffraction (EBSD, Oxford) techniques. The sample surface was mechanically ground, polished, and etched for OM and SEM observations. A specimen for EBSD scan was electropolished using a 10 vol% perchloric acid alcohol solution at the temperature of -30 °C for 150 s, with a voltage of 30 V and a current of 0.3 A. The acceleration voltage for EBSD testing was set as 20 kV with a step size of 1  $\mu$ m. Phase constitution analysis of the material was carried out by X-ray diffractometer (XRD, Shimadzu) with a scanning speed of 2° min<sup>-1</sup>. Elemental analysis was conducted using electron probe microanalysis (EPMA, Shimadzu). The MTS (C45.5.4Y) electronic universal testing machine was used for tensile tests of the materials with a gauge dimension of  $35 \times 6 \times 1$  mm<sup>3</sup>. A strain rate of  $2 \times 10^{-4}$  s<sup>-1</sup> was used for tensile tests.

#### Results and discussion Microstructural features near the Weld joint

Microstructure of the welded material was characterized with EBSD to reveal the grain structure and texture across the welding joint. Figure 1a presents the EBSD inverse pole figure (IPF) map of the welded joint, revealing distinct grain structures across different regions. An enlarged area of interest from Fig. 1a is shown in Fig. 1b, where three regions of grain structure can be discerned. The base material (BM, Region I) demonstrates an equiaxed grain morphology with an average grain size of 7.2  $\mu$ m. The fusion zone (FZ) comprises of columnar grains (Region II) and coarse equiaxed grains (Region III) with an average grain size of 23.2  $\mu$ m and 38.8  $\mu$ m, respectively (shown in Fig. 1c). The BM exhibits a typical extrusion texture where most of the grains orientated with their basal planes normal to ND, as shown in Fig. 1d. Pole figures (PFs) of the FZ reveal a relatively random grain orientation that could be resulted from the solidification crystallization during the welding process.

The grain structure formed in the FZ is similar to the macrostructure zone in a practical cast ingot, where central equiaxial grain and columnar crystals typically occur. During the laser welding process, liquid metal at the boundary of FZ/BM firstly starts to nucleate because of the low temperature away from the center of the FZ. The temperature difference between the front of crystal and liquid decreases and it is difficult to nucleate new crystals, and hence crystallization continues through growing old nuclei. Because of the limitation of heat releasing direction, growing direction of crystals is toward the center of FZ, columnar grains form. As columnar crystals grow, temperature difference between the front of crystal and liquid reduces, resulting in the stop of columnar crystals growth. Further solidification in the center of FZ needs nucleating and growing independently in the liquid of central zone. As a result, equiaxed grains form in the center<sup>20</sup>.

In order to clarify the formation of secondary phase during the laser welding process, microstructures of the welding joint were further characterized with SEM and EPMA. Three different zones, namely BM, heat affected zone (HAZ), and FZ, were divided across the weld joint based on the microstructure characteristics shown in Fig. 2a. No precipitates were observed in the BM from the SE image. Microstructure from the interfacial zone between BM and FZ, here defined as HAZ, displays an equiaxed grain structure but with a large number of precipitates and coarsened grain boundaries. The width of the HAZ is approximately  $60 \mu m$ . Both the amount

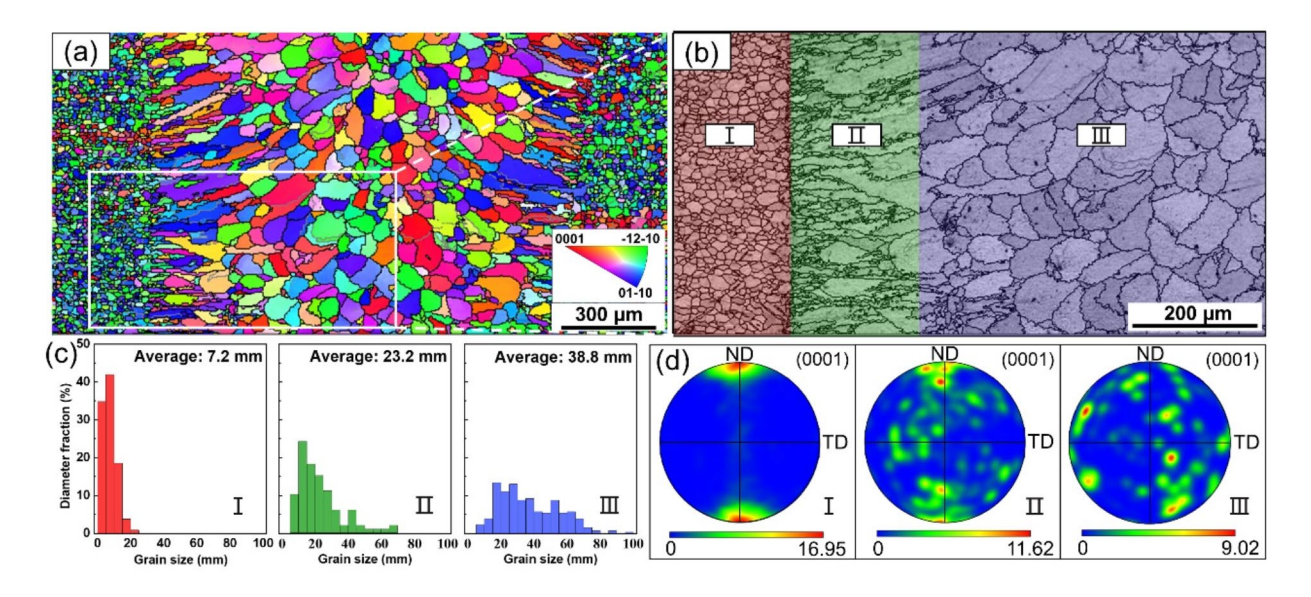


Fig. 1. EBSD microstructure of the AZ80 Mg alloy welded joint: (a) Inverse pole figure (IPF) map, (b) image quality map of an enlarged area of interest from (a), (c) grain size distribution across different regions, and (d) pole figures (PFs) of different regions illustrated in (b).

and size of precipitates vary across the width of HAZ due to the temperature difference across the welding zone during solidification, likening a heat treatment effect on the BM. The FZ features a distinct network structure of secondary phase, both in the regions of columnar grains and in the center equiaxed grains. EPMA elemental mapping of the HAZ and FZ reveal both the precipitates and secondary phase contain a high content of Al element, with a uniform distribution of Zn element, as shown in Fig. 2b and c. The network structure of the secondary phase in the FZ forms is own to be Al segregation during the rapid solidification process of the material in laser welding.

#### Mechanical properties of the welded material

Figure 3a compares the engineering stress-strain curves of the as welded material and the base material. The welded material maintains a high level of yield stress (YS) and ultimate tensile strength (UTS), as shown in Table 1. The quality of welded joints is usually evaluated by joint efficiency,  $\eta^{21}$ :

$$\eta = \frac{\sigma_w}{\sigma_B} \tag{1}$$

where  $\sigma_w$  is the tensile strength of the welded sample,  $\sigma_B$  is the tensile strength of the base material. The joint efficiency of the laser welding AZ80 Mg alloy in this study achieves 92%, indicating excellent weldability of the material. The YS of most Mg alloy welded joints is lower than that of the base materials, which may be caused by the changed microstructure of the joint during the welding process.

Several factors affect the yield strength of a material. First of all, the grain size effect according to the Hall-Petch relationship<sup>22</sup>:

$$\sigma = \sigma_0 + kd^{-1/2} \tag{2}$$

where  $\sigma_0$  is the lattice friction force that needs to be overcome to move a single dislocation, k is a coefficient and d is the grain size. The YS of polycrystalline materials is inversely proportional to the square root of grain size. In the case of the laser welding AZ80 Mg alloy, the coarsened grains in the FZ would deteriorate the mechanical strength of the material. Another factor that could affect the YS is texture strengthening. As shown in Fig. 1d, the BM exhibits a strong basal texture that is not conducive to basal slip activation, while in the FZ, the random texture favors the activation of basal slip. Given that the critical resolved shear stress (CRSS) for basal plane slip is significantly lower than for non-basal slip<sup>23</sup>, the FZ exhibits a weaker texture strengthening effect.

Despite an increase in average grain size and weakening texture of the FZ in the welded material, the YS of the laser welding AZ80 Mg alloy remains comparable to that of the BM. However, precipitates introduce Orowan strengthening by hindering dislocation movement during plastic deformation<sup>24</sup>, thereby improving the strength of the welding joint. In addition, hetero-deformation induced (HDI) stress strengthening<sup>25,26</sup> may also contribute to the strengthening of the welded material, owing to the significant difference in microstructure between the FZ and the BM (as shown in Figs. 1a and 2a). In this regard, the structural difference could cause inhomogeneous deformation in different zones of the welded material, leading to an increased dislocation density in the joint geometry, thereby improving the strength of the joint. Both of the precipitation and heterostructure in the welding joint increase the dislocation density during the tensile deformation, leading to an enhanced work-

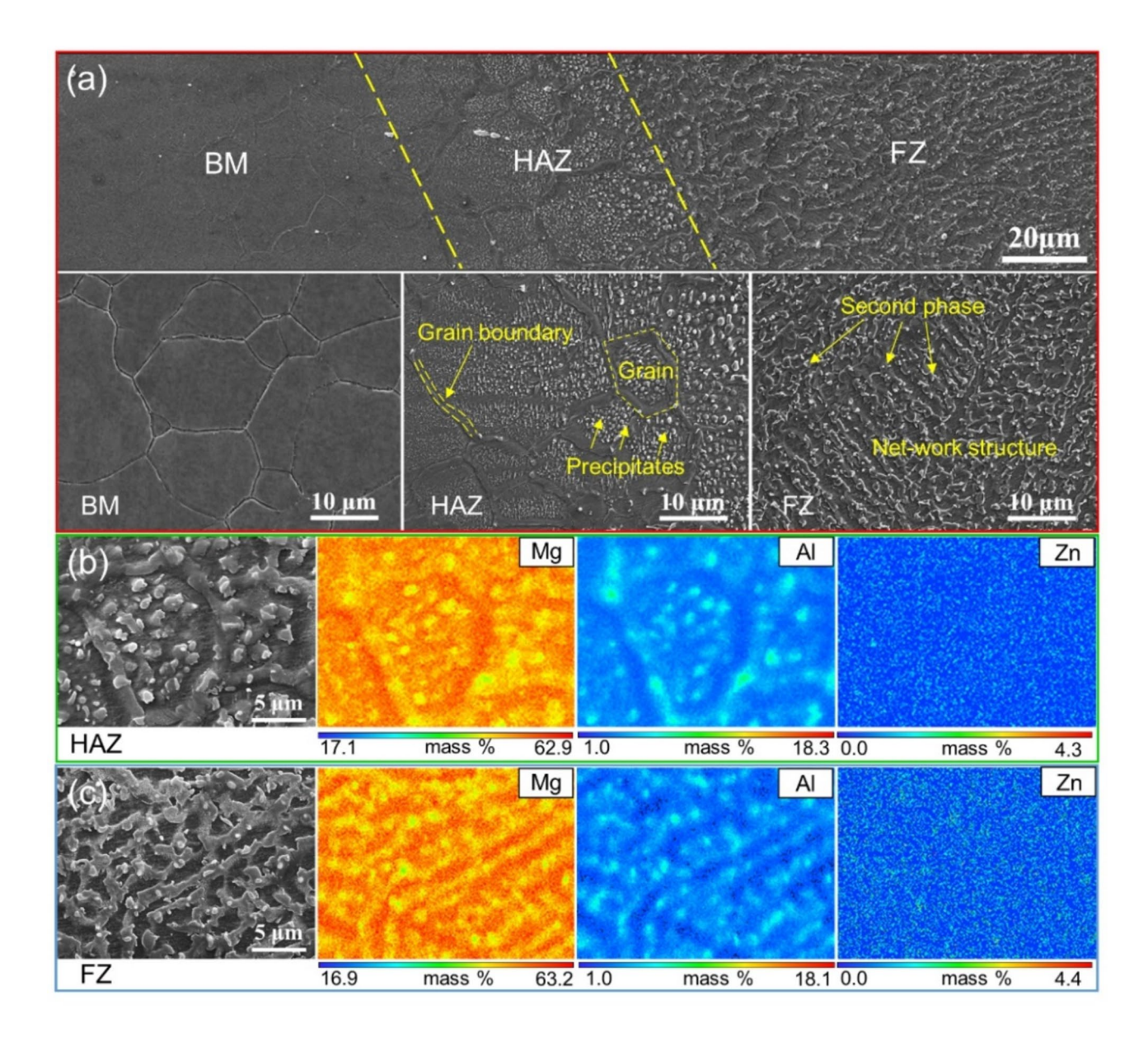


**Fig. 2.** Secondary electron (SE) images and EPMA elemental mapping of the welding joint: (a) SE images of BM, HAZ, and FZ, (b) EPMA elemental mapping of HAZ, and (c) EPMA elemental mapping of FZ.

hardening rate of the welded material. The yield strength and joint efficiency of typical Mg alloys are compared, as shown in Fig. 3b<sup>14,15,27-40</sup>. The data reveal a generally inverse relationship between yield strength and joint efficiency in welded Mg alloys. In this study, the AZ80 Mg alloy exhibited exceptional performance in both yield strength and joint efficiency.

#### Mechanisms of strength retention in welded joints

To explore the mechanisms behind the retention of joint strength, a synchrotron X-ray diffraction line scan was performed on the as-welded material. The heat map results from the line scan, shown in Fig. 4a, indicate that Mg is the solely existing phase in the BM regions. However, in the FZ, two  $Mg_{17}Al_{12}$  diffraction peaks were detected, indicating precipitation occurs during the cooling process post-welding, consistent with the Al-rich phase observed in Fig. 2b and c. A narrow transition zone between the BM and FZ, approximately 150  $\mu$ m wide was observed in X-ray diffraction scan line. Given that the synchrotron X-ray beam size is  $150 \times 150 \ \mu$ m², larger than the scanning step size of 50  $\mu$ m and the width of the HAZ (Fig. 2a), the diffraction from a single point in this area encompasses signals from the BM, FZ, and FAZ.

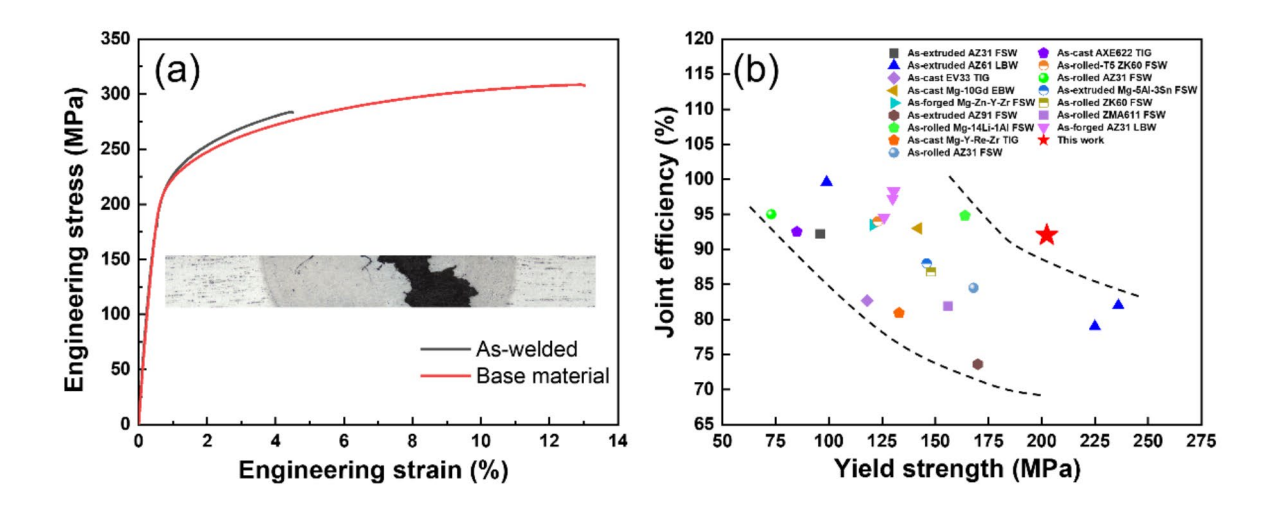


**Fig. 3.** Mechanical properties of the welded material and base material: (a) Engineering stress-strain curves, (b) relations of yield strength and joint efficiency of welded AZ80 and previously reported welded Mg alloys<sup>14,15,27–40</sup>.

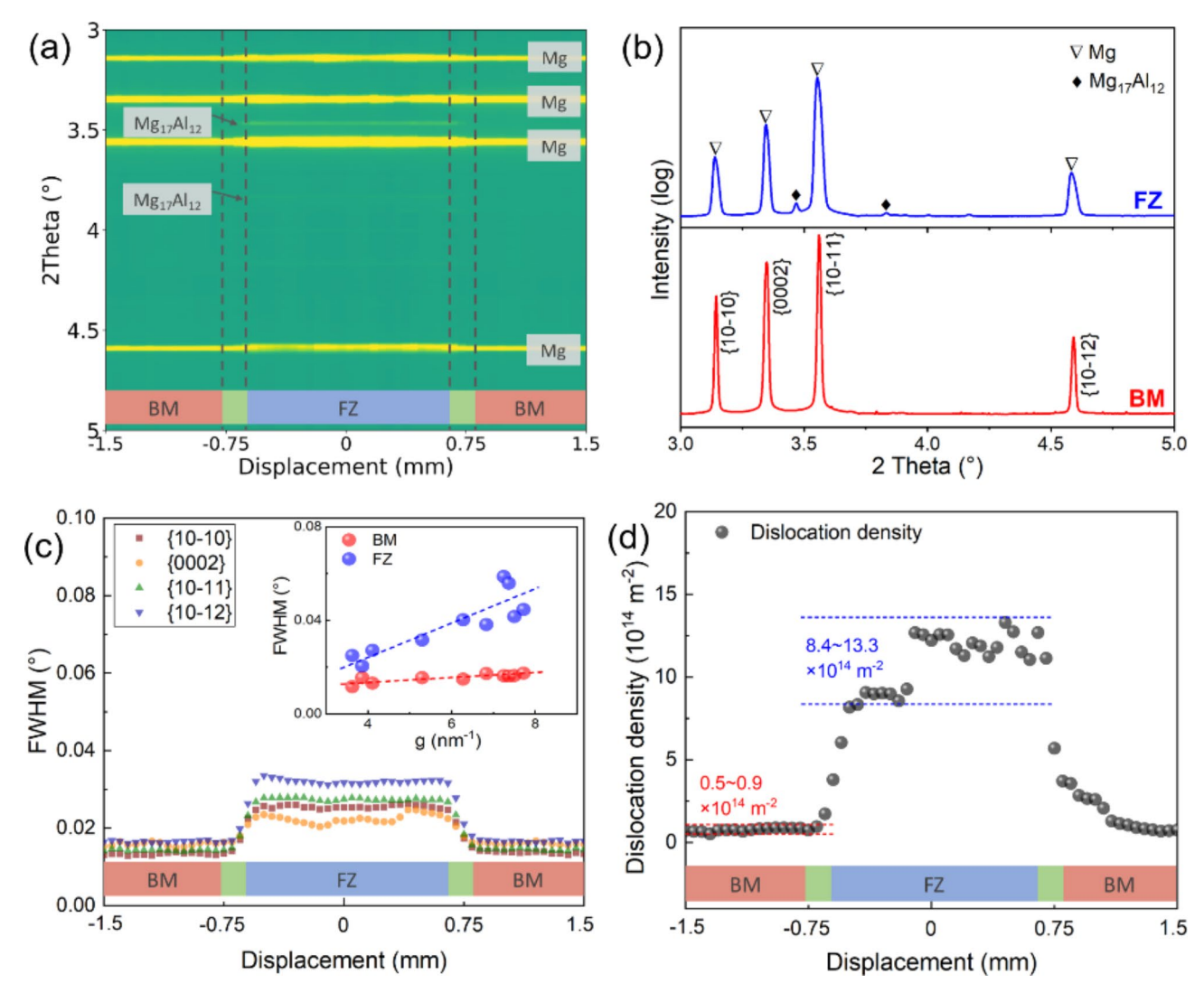
Material	Yield strength (MPa)	Ultimate tensile strength (MPa)	Elongation (%)	Joint efficiency (%)
As-welded	202.4	284.0	4.49	92.03
Base material	205.8	308.6	13.02	100

Table 1. Mechanical properties and joint efficiency of the welded material and base material.

Figure 4b shows the X-ray diffraction profiles for both the BM and FZ regions, revealing the formation of Mg<sub>17</sub>Al<sub>12</sub> phase in the FZ. Additionally, the diffraction peaks in the FZ broaden compared with in the BM. The full width at half maximum (FWHM) for four diffraction peaks ({10-10}, {0002}, {10-11}, and {10-12}) was analyzed along the line scan direction, as shown in Fig. 4c. The FWHM values range from 0.012° to 0.018° in the BM. In contrast, the FWHM values were significantly increased and exhibited greater variation in the FZ, ranging from 0.020° to 0.035°. Williamson-Hall (W-H) method was used to study the relationship between peak width and g vectors ( $g = d^{-1}$ , where d is the spacing of the considered diffraction planes). The insert figure in Fig. 4c plots the FWHM against g vectors for ten diffraction peaks selected from the BM and FZ, respectively. The W-H slope for the BM was found to be  $9.0 \times 10^{-40}$  nm, while in the FZ, it was significantly increased to 6.8×10<sup>-30</sup> nm. According to W-H theory, changes in the slope are primarily attributed to microstrain from dislocation-like defects<sup>41</sup>, indicating a substantial higher dislocation density in the FZ. The dislocation densities around the welding joint were calculated using the convolutional multiple whole profile (CMWP) method (Fig. 4d), resulting in values of  $0.5 \sim 0.9 \times 10^{14}$  m<sup>-1</sup> for BM and  $8.4 \sim 13.3 \times 10^{14}$  m<sup>-1</sup> for FZ. It is noteworthy that the increase in the peak width of the FZ region is not solely attributable to the rise in dislocation density; it is also undeniably influenced by residual stress. During the cooling process following welding, the temperature gradient generates residual stress in the vicinity of the joint 42,43. This residual stress, in conjunction with the increased dislocation density, contributes to the observed broadening of the peak width. This increase in dislocation density is consistent with the findings in 6061 Al alloys<sup>44</sup>, where friction-stir welding (FSW) was observed to increase dislocation density by a factor of seven compared to the base material. In this study, the increased dislocation density serves as an additional strengthening mechanism, alongside precipitation hardening, contributing to the enhanced strength of the welded material.

#### Conclusions

In summary, this study demonstrates the heterogeneous microstructure and strengthening mechanisms in a laser-welded AZ80 Mg alloy. The investigation revealed that the welding process resulted in the formation of a coarse-grained fusion zone (FZ) with a continuous network of secondary phases. In the heat-affected zone (HAZ),  $Mg_{17}Al_{12}$  precipitates and grain boundary coarsening were observed. The welded joint exhibited superior mechanical properties, achieving a joint efficiency of 92%. Microstructural analysis using EPMA, EBSD, and synchrotron X-ray diffraction highlighted the key strengthening mechanisms. The primary factors contributing to the high strength of the laser-welded AZ80 Mg alloy were the increased dislocation density and the presence of precipitates within the FZ. The mechanical strength of the as-welded material is comparable to that of BM owing to the strengthening mechanisms of Orowan strengthening, hetero-deformation induced (HDI) stress, and strain hardening.



**Fig. 4.** Synchrotron X-ray diffraction analysis in the welding joint: (a) Diffraction heat map around a welding joint, (b) Integrated diffraction profiles of BM, and FZ, (c) FWHM evolution of four selected Mg peaks, insert is the Williamson-Hall (WH) plots for Mg peaks at BM, and FZ, and (d) Dislocation densities determined by the convolutional multiple whole profile (CMWP) method.

#### Data availability

Data is available on request from the authors, and individuals seeking access may communicate with the corresponding author for further assistance.

Received: 25 June 2024; Accepted: 20 September 2024 Published online: 03 October 2024

#### References

- 1. Jian, W. W. et al. Ultrastrong mg alloy via nano-spaced stacking faults. Mater. Res. Lett. 1(2), 61-66 (2013).
- 2. Wang, J. et al. Strengthening mechanisms, hardening/softening behavior, and microstructure evolution in an LPSO magnesium alloy at elevated temperatures. *Mater. Charact.* **203**, 113066 (2023).
- Zhang, L. et al. Thermal conductivity and mechanical properties of graphite/Mg composite with a super-nano CaCO<sub>3</sub> interfacial layer. iScience 26, 4 (2023).
- 4. Naik, B. S., Chen, D. L., Cao, X. & Wanjara, P. Microstructure and fatigue properties of a friction stir lap welded magnesium alloy. *Metall. Mater. Trans. A* 44(8), 3732–3746 (2013).
- Miao, Y., Han, D. F., Yao, J. Z. & Li, F. Effect of laser offsets on joint performance of laser penetration brazing for magnesium alloy and steel. Mater. Des. 31, 3121–3126 (2010).
- Dorbane, A. et al. Microstructural observations and tensile fracture behavior of FSW twin roll cast AZ31 mg sheets. Mat. Sci. Eng. A 649, 190–200 (2016).
- 7. Zhang, H. J., Guo, B. S., Du, W. B., Cong, X. Y. & Chen, C. Study on the weld formation, microstructure and mechanical properties of AZ31B mg alloy in AC/DC mixed gas tungsten arc welding process. *J. Mater. Res. Technol.* **18**, 3664–3672 (2022).
- 8. Ma, Y. R. et al. Analysis of the response of thermal-affect and multiplex strengthening mechanisms of Mg-10Gd electron beam welded joint. *Mat. Sci. Eng. A* **853**, 143608 (2022).

- 9. Balasubramanian, V. Relationship between base metal properties and friction stir welding process parameters. Mat. Sci. Eng. A 480(1), 397-403 (2008)
- Vyskoč, M., Novaković, M., Potočnik, J., Kovačocy, P. & Jurči, P. Microstructure—properties relationship in laser-welded AZ31B magnesium alloy. Mater. Charact. 208, 113664 (2024).
- 11. Zhou, J., Jia, L., He, C., Chen, Y. & Long Numerical study of heat and mass transfer in dissimilar laser welding of Mg/Al lap-joint with Ti interlayer. Int. J. Therm. Sci. 199, 108932 (2024)
- 12. Liu, Y. Q. et al. Research advances on weldability of mg alloy and other metals worldwide in recent 20 years. J. Mater. Res. Technol. 25, 3458-3481 (2023).
- 13. Cui, M. F., Zheng, Z. T., Du, P. & Chang, L. A double molten pool laser welding process for joining magnesium alloys and aluminum alloys: the process, microstructure and mechanical properties of joints. Mater. Today Commun. 35, 106116 (2023).
- 14. Shan, J. Laser Welding of Magnesium Alloys 306-350 (Woodhead Publishing, 2010).
- 15. Shen, J., Wen, L., Li, Y. & Min, D. Effects of welding speed on the microstructures and mechanical properties of laser welded AZ61 magnesium alloy joints. Mat. Sci. Eng. A 578, 303-309 (2013).
- 16. SHi, Y. B. Effect of laser welding process parameters on properties of AM80 magnesium alloy welded joint. Ordnance Mat. Sci. Eng. 44(4), 97-101 (2021).
- 17. Min, D., Shen, J., Lai, S. Q. & Chen, J. Effect of heat input on the microstructure and mechanical properties of tungsten inert gas arc butt-welded AZ61 magnesium alloy plates. Mater. Charact. 60(12), 1583-1590 (2009).
- 18. Park, S. H. C., Sato, Y. S. & Kokawa, H. Effect of micro-texture on fracture location in friction stir weld of mg alloy AZ61 during tensile test. Scripta Mater. 49(2), 161-166 (2003).
- 19. Singh, K., Singh, G. & Singh, H. Review on friction stir welding of magnesium alloys. J. Magnes Alloys 6(4), 399-416 (2018).
- 20. Glicksman, M. E. Principles of Solidification: An Introduction to Modern Casting and Crystal Growth Concepts (Springer Science & Business Media, 2010).
- 21. Cao, X., Jahazi, M., Immarigeon, J. P. & Wallace, W. A review of laser welding techniques for magnesium alloys. J. Mater. Process. Tech. 171(2), 188-204 (2006).
- 22. Zhu, G. M. et al. Grain-size effect on the deformation of Mg-3Al-3Sn alloy: experiments and elastic-viscoplastic self-consistent modeling. Int. J. Plast. 143, 103018 (2021).
- 23. Dan, Y. & Trinkle, D. R. First-principles core energies of isolated basal and prism screw dislocations in magnesium. Mater. Res. Lett. 10(6), 360-368 (2022).
- 24. Pan, H. C. et al. Development of low-alloyed and rare-earth-free magnesium alloys having ultra-high strength. Acta Mater. 149, 350-363 (2018).
- 25. Zhu, Y. T. & Wu, X. L. Perspective on hetero-deformation induced (HDI) hardening and back stress. Mater. Res. Lett. 7(10), 393-398 (2019).
- 26. Yang, M. X., Pan, Y., Yuan, F. P., Zhu, Y. T. & Wu, X. L. Back stress strengthening and strain hardening in gradient structure. Mater. Res. Lett. 4(3), 145-151 (2016).
- 27. Shang, Q., Ni, D. R., Xue, P., Xiao, B. L. & Ma, Z. Y. Improving joint performance of friction stir welded wrought mg alloy by controlling non-uniform deformation behavior. Mat. Sci. Eng. A 707, 426-434 (2017).
- 28. Wang, Q. et al. Microstructure and strengthening mechanism of TIG welded joints of a Mg-Nd-Gd alloy: effects of heat input and pulse current. Mat. Sci. Eng. A 869, 56 (2023).
- 29. Ma, Y. et al. Analysis of the response of thermal-affect and multiplex strengthening mechanisms of Mg-10Gd electron beam welded joint. Mat. Sci. Eng. A 2022, 853 (2022).
- 30. Xie, G. M., Ma, Z. Y., Geng, L. & Chen, R. S. Microstructural evolution and mechanical properties of friction stir welded Mg-Zn-Y-Zr alloy. Mat. Sci. Eng. A 471(1-2), 63-68 (2007).
- 31. Singh, K. & Kumar Sehgal, A. Evaluation of characteristics of friction stir welded Mg-Al-Zn magnesium alloy. Mater. Today: Proc. **78**, 437–443 (2023).
- 32. Xu, N. et al. Y.-f. Bao, enhanced strength and ductility of rapid cooling friction stir welded ultralight Mg-14Li-1Al alloy joint. J. Mater. Res. Technol. 23, 4444-4453 (2023).
- 33. Tong, X. et al. Microstructure and mechanical properties of repair welds of low-pressure sand-cast Mg-Y-RE-Zr alloy by tungsten inert gas welding. J. Magnes Alloys 10(1), 180-194 (2022).
- 34. Chen, S. et al. Microstructure and mechanical properties of AZ31B mg alloy fabricated by friction stir welding with pulse current. J. Manuf. Process. 71, 317-328 (2021).
- 35. Eftekhar, A. H., Sadrossadat, S. M. & Reihanian, M. Effect of heat input on microstructure and mechanical properties of TIGwelded semisolid cast AXE622 mg alloy. Mater. Charact. 2022, 184 (2022).
- 36. Li, G. H. et al. Evolution of grain structure, texture and mechanical properties of a Mg-Zn-Zr alloy in bobbin friction stir welding. Mat. Sci. Eng. A 799, 896 (2021).
- 37. Xin, R. et al. Influence of welding parameter on texture distribution and plastic deformation behavior of as-rolled AZ31 mg alloys. J. Alloy Compd. 670, 64-71 (2016)
- 38. Pan, F. et al. Effects of friction stir welding on microstructure and mechanical properties of magnesium alloy Mg-5Al-3Sn. Mater. Des. 110, 266-274 (2016).
- 39. Li, G. H., Zhou, L., Luo, S. F., Dong, F. B. & Guo, N. Quality improvement of bobbin tool friction stir welds in Mg-Zn-Zr alloy by adjusting tool geometry. J. Mater. Process. Tech. 2020, 282 (2020).
- 40. Kim, B. et al. Microstructure and mechanical properties of twin-roll cast Mg-6Zn-1Mn-1Al alloy joined by surface-friction welding. Mater. Charact. 124, 8-13 (2017).
- 41. Wang, J. et al. Understanding the high strength and good ductility in LPSO-containing mg Alloy using synchrotron X-ray diffraction. Metall. Mater. Trans. A 49(11), 5382-5392 (2018).
- 42. Radaj, D. Heat Effects of Welding: Temperature Field, Residual Stress, Distortion (Springer Science & Business Media, 2012).
- 43. Romero, J., Attallah, M. M., Preuss, M., Karadge, M. & Bray, S. E. Effect of the forging pressure on the microstructure and residual stress development in Ti-6Al-4V linear friction welds. Acta Mater. 57(18), 5582-5592 (2009).
- 44. Woo, W., Ungár, T., Feng, Z. L., Kenik, E. & Clausen, B. X-Ray and Neutron Diffraction measurements of dislocation density and subgrain size in a friction-stir-welded aluminum Alloy. Metall. Mater. Trans. A 41(5), 1210-1216 (2010).

#### Acknowledgements

This work was financially supported by the National Natural Science Foundation of China (No. 52425101, 52301018). The authors are thankful for the kind help of Li Li at the Teaching Laboratory Center for School of Materials Science and Engineering of Shanghai Jiao Tong University. We acknowledge DESY (Hamburg, Germany), a member of the Helmholtz Association HGF, for the provision of experimental facilities. Parts of this research were carried out at the PETRA III beamline P21.2.

#### Author contributions

Y. Liu: Investigation, Methodology, Writing - Original Draft, Formal analysis. G. Zhu: Investigation, Supervi-

Scientific Reports |

sion, Writing - Review & Editing, Funding acquisition. Y. Wang: Methodology. Z. Xin: Investigation. N. Hao: Investigation. W. Huang: Investigation. S. Yi: Writing - Review & Editing. D. Letzig: Resources. U. Lienert: Resources, Writing - Review & Editing. J. Wang: Investigation, Supervision, Resources, Writing - Review & Editing. X. Zeng: Supervision, Funding acquisition, Writing - Review & Editing. All authors reviewed the manuscript.

#### Competing interests

The authors declare no competing interests.

#### Additional information

**Supplementary Information** The online version contains supplementary material available at https://doi.org/10.1038/s41598-024-73767-0.

Correspondence and requests for materials should be addressed to G.Z., J.W. or X.Z.

Reprints and permissions information is available at www.nature.com/reprints.

**Publisher's note** Springer Nature remains neutral with regard to jurisdictional claims in published maps and institutional affiliations.

Open Access This article is licensed under a Creative Commons Attribution-NonCommercial-NoDerivatives 4.0 International License, which permits any non-commercial use, sharing, distribution and reproduction in any medium or format, as long as you give appropriate credit to the original author(s) and the source, provide a link to the Creative Commons licence, and indicate if you modified the licensed material. You do not have permission under this licence to share adapted material derived from this article or parts of it. The images or other third party material in this article are included in the article's Creative Commons licence, unless indicated otherwise in a credit line to the material. If material is not included in the article's Creative Commons licence and your intended use is not permitted by statutory regulation or exceeds the permitted use, you will need to obtain permission directly from the copyright holder. To view a copy of this licence, visit <a href="http://creativecommons.org/licenses/by-nc-nd/4.0/">http://creativecommons.org/licenses/by-nc-nd/4.0/</a>.

© The Author(s) 2024